Design and Implementation of an Electrostatic Adhesion-Driven Self-Sensing Actuator for Rapid, Stiffness-Modulated Pneumatic Actuators

Hao Liu[®], Yujin Dai[®], Jia Yu, Ting Wang, and Hongqiang Wang[®], Senior Member, IEEE

Abstract-Clutches and variable stiffness actuators based on flexible electrostatic adhesion films are widely used in the field of soft robotics. Enabling sensing capabilities in these actuators can significantly enhance their environmental interaction and control performance. However, current external sensing solutions for those actuators face several challenges, including the mechanical mismatch between sensors and the soft actuators, as well as increased system complexity due to additional sensing components. This letter proposes a self-sensing scheme for an electrostatic adhesion-driven variable stiffness clutch, utilizing a capacitancebased principle to achieve position self-sensing. In addition, the pneumatic actuator fabricated based on this actuator can achieve angular sensing, rapid response, and stiffness modulation. Finally, a two-degree of freedom pneumatic variable stiffness robotic arm integrated position sensing is fabricated, which can achieve decoupled position control through a single air source.

Index Terms—Soft sensors and actuators, hydraulic/pneumatic actuators, grippers and other end-effectors.

I. INTRODUCTION

LECTROSTATIC adhesion (EA) structures have been widely applied in the field of soft robotics due to their advantages such as low weight, fast response speed, and low energy consumption [1]. In soft robotics applications, one type of electrostatic adhesion structure is used in object grasping [2]. By utilizing the principle of EA, it adheres to the objects to be grasped, thereby improving the grasping efficiency [3], [4]. The other type of EA structure is mainly applied in the fields of clutches and variable stiffness actuators [5], [6], [7], [8]. Typically, two or more layers of EA films are stacked. By controlling

Received 27 April 2025; accepted 10 September 2025. Date of publication 24 September 2025; date of current version 10 October 2025. This article was recommended for publication by Associate Editor J. Zhu and Editor C. Laschi upon evaluation of the reviewers' comments. This work was supported in part by the Natural Science Foundation of China under Grant 52275021 and Grant 52450323, in part by the Natural Science Foundation of Guangdong Province of China under Grant 2024A1515010183, and in part by Guangdong Provincial Research Support Program under Grant 2019QN01Z733. (Corresponding author: Hongqiang Wang.)

Hao Liu, Yujin Dai, Jia Yu, and Ting Wang are with the Shenzhen Key Laboratory of Biomimetic Robotics and Intelligent Systems, Southern University of Science and Technology, Shenzhen 518055, China.

Hongqiang Wang is with the Shenzhen Key Laboratory of Biomimetic Robotics and Intelligent Systems, Department of Mechanical and Energy Engineering and Guangdong Provincial Key Laboratory of Human-Augmentation and Rehabilitation Robotics in Universities, Southern University of Science and Technology, Shenzhen 518055, China (e-mail: wanghq6@sustech.edu.cn).

This article has supplementary downloadable material available at https://doi.org/10.1109/LRA.2025.3614021, provided by the authors.

Digital Object Identifier 10.1109/LRA.2025.3614021

the EA force between the films, the switching between locking and releasing or the change in the stiffness of the actuator can be realized [9], [10], [11]. During the use of the actuator, it is often accompanied by the relative displacement between the EA films [5], [10], [12]. During this process, it is very important to sense the force and displacement changes to achieve accurate control of the actuator [12], [13], [14].

However, because of the characteristics of the EA structure such as flexibility and large deformation, it poses a serious challenge to the existing sensing technologies [15], [16], [17]. Current external sensing solutions have notable limitations. Although closed-loop control can be achieved using laser displacement sensors, these additional sensors are rigid and bulky, and they cannot accurately measure displacements during bending processes [18]. While flexible resistive sensors can adapt to the deformation of soft structures to some extent, their complex structural designs and unstable reliability limit their large-scale applications [19]. Therefore, a more cost-effective and integrated sensing method is needed. Although an innovative approach involving the imprinting of moiré patterns on flexible films combined with optical sensors can achieve position sensing, this solution requires additional sensing components, thereby significantly increases the system complexity [20].

Given the limitations of existing sensing technologies in terms of cost, integration, and reliability, this letter proposes a selfsensing solution to achieve position sensing of the EA actuator. We developed an EA-driven self-sensing (EAS) actuator. The actuator comprises two EA layers that form a parallel plate capacitor. The equivalent capacitance of the actuator is directly proportional to the overlapping area of the electrodes, enabling its application in displacement sensing. Besides, the EA force can be modulated by changing the duty cycle of the excitation voltage. By integrating this actuator with a pneumatic actuator, the pneumatic actuator can achieve angle sensing and stiffness modulation. In addition, the pneumatic actuator realizes closedloop position control through a PID controller based on angle sensing. A gripper composed of pneumatic actuators can rapidly catch a falling ball within 40 ms. Through stiffness adjustment, the gripper can still achieve gripping and releasing of objects after fast response. Moreover, through stiffness control by the EAS actuator, a 2-degree of freedom (DOFs) arm controlled by a single air source has been developed. Controlling multiple joints with a single air source reduces the reliance on bulky pneumatic control modules [21].

2377-3766 © 2025 IEEE. All rights reserved, including rights for text and data mining, and training of artificial intelligence and similar technologies. Personal use is permitted, but republication/redistribution requires IEEE permission. See https://www.ieee.org/publications/rights/index.html for more information.

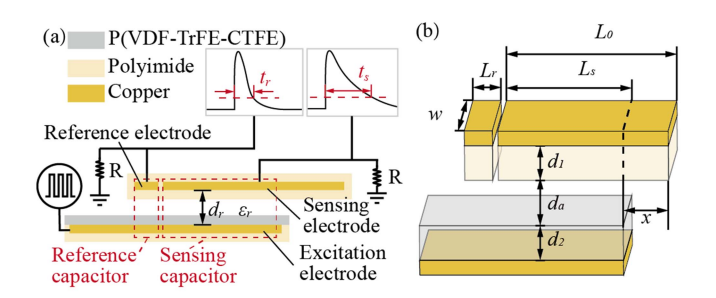


Fig. 1. (a) The schematic diagram of EAS actuator. (b) The structure of the EAS actuator.

The letter is organized as follows: Section II presents the modeling of the EAS actuator and the pneumatic actuator. Section III describes the fabrication process of the pneumatic actuator and the circuit design. Section IV presents the experimental results and demonstrations of the actuators. Section V provides the discussion of this study. Section VI provides the conclusion and future work of this study.

II. MODELING

A. The EAS Actuator Sensing Model

The structure of the EAS actuator is shown in Fig. 1. The structure consists of two electrode film layers. There are two electrodes on the upper layer, and the electrodes are covered with a piece of polyimide (PI) film (25 μ m) on both sides. One of the electrodes serves as the reference electrode, and the other is the sensing electrode. These two electrodes are sequentially positioned on the film. The lower plate includes an excitation electrode. In this work, we tested two types of coating materials on the upper side of the excitation electrode. Type A is coating a poly(vinylidene-fluoride-trifluoroethylenechlorotrifluoroethylene) [P(VDF-TrFE-CTFE)] [22] film (20 μ m), and Type B is without coating, where the electrode is directly contact with air. The lower side of the excitation electrode is covered with a 20 μ m thick PI film. The two electrode films form two parallel-plate capacitors: the reference capacitor (consisting of the reference electrode, the excitation electrode, and the insulation layers) and the sensing capacitor (consisting of the sensing electrode, the excitation electrode, and the insulation layers). When a relative displacement happens between the upper and lower films, the capacitance of the sensing capacitor will change due to the variations in the overlapping area between its electrodes. In contrast, the capacitance of the reference capacitor remains unchanged (the overlapping area is fixed and equivalent to the area of the reference electrode).

We have established a model to analyze the properties of the EAS actuator. The equivalent sensing capacitor and resistance form an RC circuit (Fig. 1(a)). Thus, the discharging process of the sensor can be equivalent to an RC circuit, and the voltage V_s across the resistor R in the sensing circuit with time t_s can be expressed as:

$$V_s = V_u e^{-\frac{t_s}{RC}},\tag{1}$$

where V_u is the initial voltage on the sensing capacitor, $C = \varepsilon_0 \varepsilon_r w L_s/d_r$ is the capacitance of the sensing capacitor, ε_0 is the permittivity of vacuum $(8.854 \times 10^{-12} F/m)$, ε_r is the relative permittivity, w is the equivalent electrode width of the capacitor, L_s is the equivalent electrode length of the capacitor, and d_r is the equivalent thickness of the insulation layers (Fig. 1).

By rearranging (1), we can get L_s . Similarly we can get the equivalent electrode length L_r of the reference capacitor:

$$L_s = \frac{t_s}{\ln\left(\frac{V_u}{V_s}\right)} \frac{\varepsilon_0 \varepsilon_r w R}{d_r}, L_r = \frac{t_r}{\ln\left(\frac{V_u}{V_s}\right)} \frac{\varepsilon_0 \varepsilon_r w R}{d_r}, \tag{2}$$

where t_r is the discharging time as the voltage across the resistor R on the reference circuit drops to V_s .

Dividing L_s by L_r , and rearranging the equation, we can obtain the displacement x of the EAS actuator:

$$x = L_0 - L_r \frac{t_s}{t_r},\tag{3}$$

where $L_0=L_s+x$ is the initial length of the sensing electrode. By measuring the discharging time t_s and t_r (the time of the voltage across the resistor R drop from V_u to V_s) for the voltage across the resistor R in the sensing capacitor and reference capacitor, respectively, we can obtain the displacement x of the EAS actuator.

B. The EA Force Model

In this part, we simplify the reference electrode and sensing electrode as one electrode. Thus the equivalent electrode area of the capacitor is $A=w(L_r+L_0-x)$, and the capacitor with Type A structure (PI and P(VDF-TrFE-CTFE) insulation layers and one air gap layer) can be equivalent to three capacitors connected in series (Fig. 1(b)), and the voltage between two electrodes is calculated as follows:

$$V_u = E_1 d_1 + E_2 d_2 + E_a d_a, (4)$$

where E_1 , E_2 and E_a are the electric field intensity of the PI layer, the P(VDF-TrFE-CTFE) layer and the air gap, respectively, and d_1 , d_2 and d_a are the thickness of the insulation layers of PI, P(VDF-TrFE-CTFE) and the air gap, respectively. And for Type B structure, $d_2=0$.

Besides, due to the continuity of the electric field in the boundary of two adjacent insulation layers, the electric displacement vector of the electric field satisfies:

$$\varepsilon_0 \varepsilon_1 E_1 = \varepsilon_0 \varepsilon_2 E_2 = \varepsilon_0 \varepsilon_a E_a, \tag{5}$$

where ε_1 , ε_2 and ε_a are the relative permittivity constant of PI, P(VDF-TrFE-CTFE) and air, respectively.

Based on (4) and (5), the electric field intensity of the air gap can be calculated as:

$$E_a = \frac{V_u}{\frac{\varepsilon_a}{\varepsilon_1} d_1 + \frac{\varepsilon_a}{\varepsilon_2} d_2 + d_a}.$$
 (6)

Therefore, the EA force density between the two electrode films σ_n can be calculated as [23]:

$$\sigma_n = \frac{1}{2}\varepsilon_0\varepsilon_a E_a^2 = \frac{1}{2} \frac{\varepsilon_0\varepsilon_a V_u^2}{\left(\frac{\varepsilon_a}{\varepsilon_1}d_1 + \frac{\varepsilon_a}{\varepsilon_2}d_2 + d_a\right)^2}.$$
 (7)

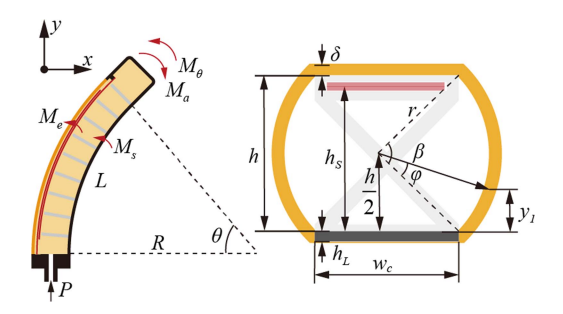


Fig. 2. Side view and cross-section view of the EAS pneumatic actuator.

Thus, we can obtain that the tangential EA force between the electrode films is:

$$F_t = \mu \sigma_n w (L_r + L_0 + x), \tag{8}$$

where μ is the friction coefficient between the insulation layers. As described in (7), the EA force is inversely proportional to the square of the distance between the two electrode layers. Therefore, reducing the electrode gap can significantly enhance the EA force under the same applied voltage, enabling a broader range of stiffness modulation. In our design, the Type B structure adopts a smaller inter-electrode gap compared to the Type A structure. This configuration partially offsets the reduction in EA force caused by the lower dielectric constant of the insulating material, thereby maintaining effective stiffness enhancement

C. The Pneumatic Actuator Design

and improving overall modulation performance.

The cross-section of the pneumatic actuator is shown in Fig. 2. According to the geometric relationship, the bending moment M_a exerted by the internal air pressure on the distal cover of the actuator is:

$$M_a = P\left(2\int_0^{\frac{\pi}{2}} \int_0^r \left(\frac{h}{2} + \beta \sin\left(\varphi - \frac{\pi}{4}\right)\right) \beta d\beta d\varphi$$
$$-2\int_0^{\frac{h}{2}} y^2 dy - 2\int_{\frac{h}{2}}^h y(h-y) dy + \int_0^h y w_c dy\right),$$

where P is the air pressure, h is the height of the actuator, β is radius increment of the arc-shape area of the actuator, φ is the angle increment of the arc-shape area of the actuator, y is the height increment of the actuator, and w_c is the bottom width of the actuator.

After simplification, we can get:

$$M_a = \frac{4w_c h^2 + (\pi - 2)h^3}{8}P. (10)$$

The elastic film of the actuator is made of incompressible latex rubber material, and is wrapped by a constraint layer made of PI on the outside. According to the soft fiber-reinforced bending actuators model [24], we can obtain the axial principal nominal force density of the actuator film as:

$$s_1 = \bar{\mu}\lambda - \frac{\bar{\mu}}{\lambda^3},\tag{11}$$

where $\bar{\mu}$ is the equivalent shear modulus, $\lambda = 1 + \delta\theta/L$ is the principal stretch ratio in the axial direction, δ is the thickness of the elastic film, θ is the bending angle of the actuator, L is the length of the neutral layer.

Therefore, the bending moment caused by the deformation of the actuator film material is:

$$M_{\theta} = \int_{h}^{h+\delta} \left(\bar{\mu} \left(1 + \frac{y\theta}{L} \right) - \frac{\bar{\mu}}{\left(1 + \frac{y\theta}{L} \right)^3} \right) w_c y dy$$
$$+ 2 \int_{0}^{\frac{\pi}{2}} \int_{r}^{r+\delta} \left(\bar{\mu} \left(1 + \frac{y_1 \theta}{L} \right) - \frac{\bar{\mu}}{\left(1 + \frac{y_1 \theta}{L} \right)^3} \right) y_1 \beta d\beta d\varphi, \tag{12}$$

where $y_1 = \frac{h}{2} + \beta \frac{\sqrt{2}}{2} (\sin \varphi - \cos \varphi)$ is the height along the y direction.

In addition, the 3D-printed skeleton (discussed in section III) also provides a bending moment during the actuator's bending process. We regard the constraint layer on the skeleton as an isotropic thin-plate material. The bending moment M_s is calculated as:

$$M_s = \frac{Ew_c h_L^3 \theta}{6L},\tag{13}$$

where E is the elastic modulus of the material, and h_L is the thickness of the thin plate.

When the actuator is bent, the two electrode films on the EAS actuator will generate an EA force, and the bending moment generated by the EA force can be calculated as follows:

$$M_e = F_t h_s, (14)$$

where h_s is the distance from the EAS actuator to the neutral layer, $F_t = \mu \sigma_n w (L_r + L_0 + \theta h_s)$, which is inversely proportional to the bending angle θ .

When the actuator is not subjected to an external force, the bending moment balance condition is satisfied:

$$M_a = M_\theta + M_s + M_e. (15)$$

Through the position self-sensing capability of the EAS actuator, the bending angle of the pneumatic actuator can be accurately estimated, providing a foundation for closed-loop position control. Based on the angle sensing, stiffness modulation at different bending angles can be achieved by adjusting the excitation voltage (e.g., the duty cycle of the excitation voltage).

III. FABRICATION

A. Fabrication of Pneumatic Actuator

The actuator structure consists of four parts: a PI constraint layer used to restrict the circumferential expansion of the actuator, a latex film, a 3D-printed skeleton, and an EAS actuator(Fig. 3). The fabrication process begins with cutting the adhesive-backed PI film (DuPont, 25 μ m thick with 50 μ m 3M 467 MP adhesive) into the desired shape using a graphic cutting machine (Cricut Maker 3) to form the constraint layer. A latex film (HBL, 0.3 mm) is then bonded to the PI layer. A PI mask film is applied to the latex surface, and adhesive (Kaibingtuan 5526) is selectively coated onto exposed areas, followed by bonding

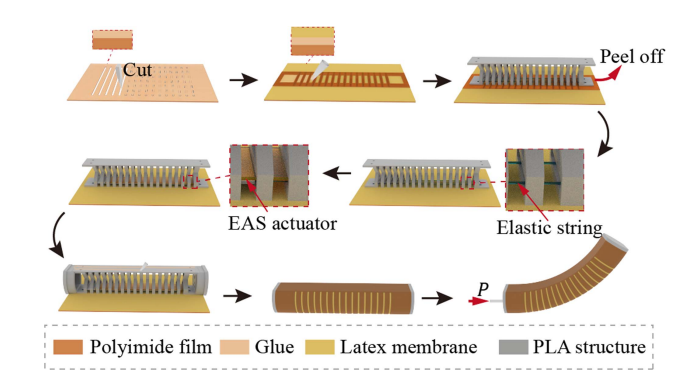


Fig. 3. The fabrication process of the EAS pneumatic actuator.

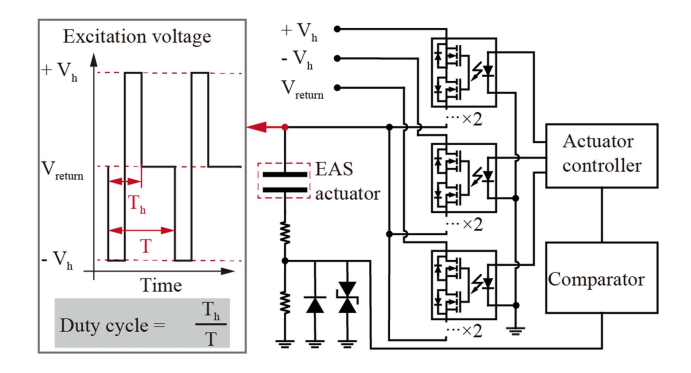


Fig. 4. The circuit of the EAS actuator.

the 3D-printed skeleton. After the adhesive cures, the mask is removed. To prevent sticking during bending, two parallel elastic strings are added to the skeleton. The EAS actuator is assembled onto the skeleton, with both ends of the films fixed in place. 3D-printed adapters are attached to both ends, and the latex–PI constraint layer is sealed onto the skeleton with adhesive. Finally, the air tube and sensing wires are installed, and the sealing performance of the actuator is tested. All the 3D-printed parts are fabricated using polylactic acid (PLA) materials.

B. Circuit Design

The circuit of the EAS actuator mainly consists of two parts: the signal excitation circuit and the signal acquisition circuit (Fig. 4). The excitation circuit comprises a high voltage module and a signal generation module. The high voltage module uses two XP Power modules (HRL3024S1K5P and HRL3024S1K5N) to generate controllable positive and negative high voltages. The signal generation module utilizes three PhotoMOS-based (Panasonic, AQV258HC8) bridges to generate high voltage square waves. Given that the maximum voltage rating of a single PhotoMOS is 1500 V, two PhotoMOS are connected in series within each bridge circuit to raise the voltage withstand level of the circuit to 3000 V.

The signal acquisition circuit converts analog to digital signals. Two voltage-dividing resistors first reduce high-voltage signals from sensing/reference capacitors to low-voltage levels. A parallel diode clamps negative voltages to near zero, and a Schottky diode at the output limits voltage to less than 3.3 V, protecting downstream circuits. A TLV3502 comparator then

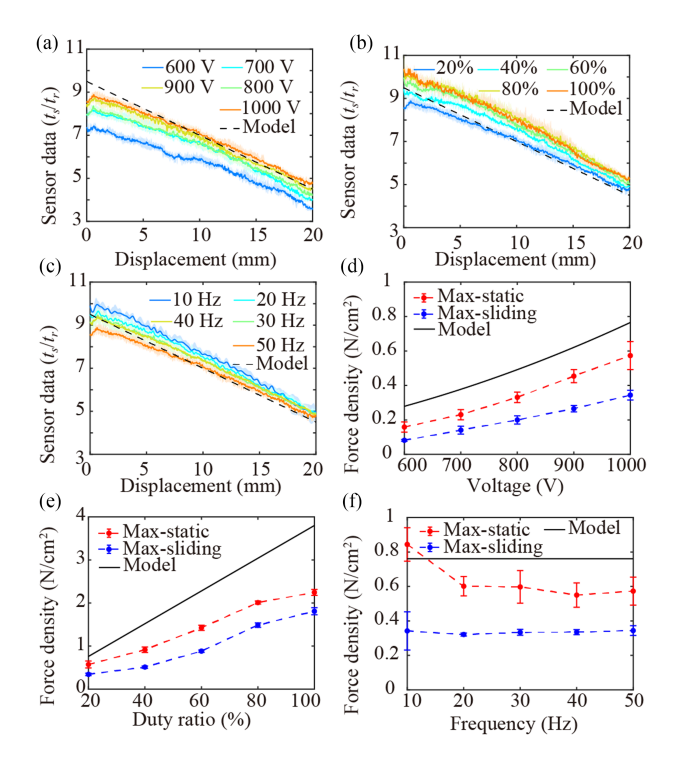


Fig. 5. The sensor data and maximum tangential EA forces density of the EAS actuator. The sensor data of the EAS actuator with displacement under different (a) excitation voltage, (b) duty cycle, and (c) excitation frequency. The maximum tangential EA force density of the EAS actuator are under different (d) excitation voltage, (e) duty cycle, and (f) excitation frequency.

generates a digital signal: high when input larger than threshold V_s , low otherwise. Finally, an ESP32S3 microcontroller converts this to a time-based signal (duration above V_s), proportional to actuator displacement via (3).

IV. EXPERIMENTS VALIDATION

A. EAS Actuator Test

This section investigates how various parameters influence the actuator's sensing performance and EA force. Owing to the high relative permittivity (up to 45) of the P(VDF-TrFE-CTFE) dielectric, the EA actuator achieves high force density [22]. All tests in this section were conducted using the Type A structure. As shown in Fig. 5(a)–(c), sensor output increased with voltage amplitude and duty cycle but decreased with frequency. Similarly, the maximum tangential static EA force density increased with amplitude and duty cycle, while frequency had minimal influence (Fig. 5(d)–(f)); the sliding EA force followed the same trend. Notably, although (3) suggests the sensor output should be independent of amplitude and duty cycle, experiments showed otherwise. This discrepancy may stem from the larger area of the sensing electrode, which amplifies capacitance changes when voltage increases. Uneven electrode contact due to larger area can cause greater electrode gap variation under changing EA force, leading to larger capacitance shifts. To balance EA force and sensing accuracy, a voltage of 1000 V, 20% duty cycle, and 50 Hz frequency were selected. Under these conditions, the actuator achieved a linearity error of 4.92% and an EA force density of 1.99 N/cm².

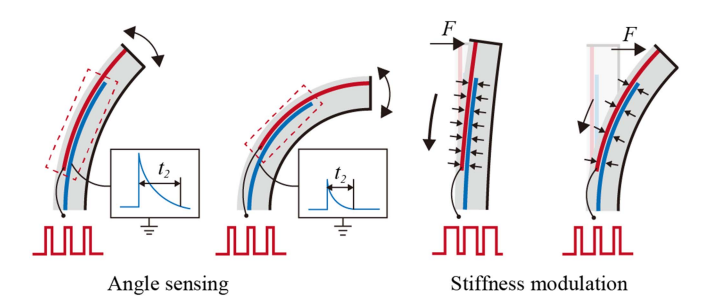


Fig. 6. The principle of self sensing and stiffness modulation of the pneumatic actuator.

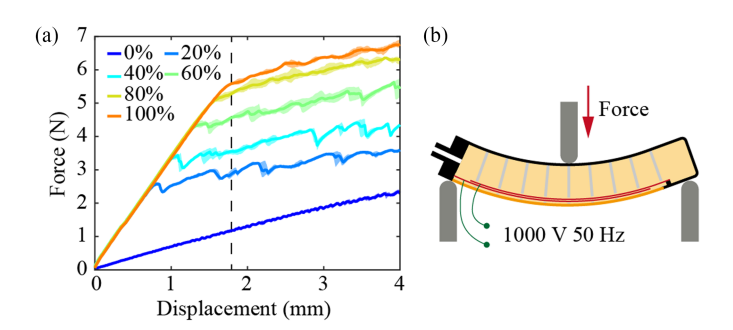


Fig. 7. (a) The Force-displacement test of the EAS pneumatic actuator under different duty cycle of the excitation voltage. (b) Schematic diagram of the test.

B. Pneumatic Actuator Test

Pneumatic actuators can achieve both angle sensing and stiffness modulation using the integrated EAS actuator (Fig. 6). During bending, the length of the EAS actuator changes, enabling angle estimation through self-sensing. Additionally, adjusting the duty cycle of the excitation voltage allows control of the EA force, thereby achieving the stiffness adjustment of the pneumatic actuator.

A three-point bending test was conducted using a tensile testing machine (MTS Criterion Model 42) to evaluate stiffness modulation. The actuator was unpressurized (0 kPa), and a 50 Hz, 1000 V excitation voltage was applied to the EAS actuator with varying duty cycles (0%–100%). Results showed that, under the same displacement (e.g., 1.8 mm), the force increased with higher duty cycles. Conversely, for the same force, higher duty cycles resulted in greater displacement before slipping occurred (Fig. 7), indicating increased stiffness with increasing duty cycle. Notably, the actuator exhibited a 4.66 times stiffness variation ratio as the duty cycle increased from 0% to 100% (based on compression at 1.8 mm) under a fast variation speed (20 ms, 50 Hz excitation voltage frequency).

The relationship between the pneumatic actuator's bending angle and air pressure was evaluated by linearly increasing the pressure from 0 kPa to 60 kPa using a proportional valve (SMC, IT1030-312 L). Bending angles were recorded using both a vision-based method and the embedded EAS actuator. For visual tracking, three markers were placed on the actuator's side, and motion was captured with a camera (Canon EOS 5D Mark IV), with angles extracted via a vision algorithm. Simultaneously, the EAS actuator (1000 V, 20% duty cycle, 50 Hz) provided real-time angle measurements. Results showed that the bending

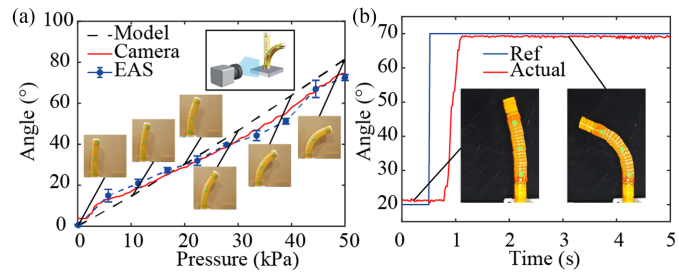


Fig. 8. (a)The bending angle of the EAS pneumatic actuator under different air pressures, compared with the bending angle acquired by the visual algorithm and the model result. (b) PID step response curve based on angle sensing.

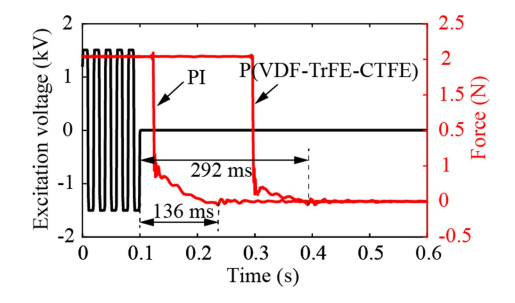


Fig. 9. The discharge response time of the EAS actuator under 200 g load.

angle increased with pressure and matched well with theoretical predictions (Fig. 8(a)).

Based on self-sensed angle data, closed-loop position control was implemented using a PID controller. The step response in Fig. 8(b) confirms accurate position tracking, demonstrating the effectiveness of the integrated sensing-feedback loop.

C. Locking and Sensing Modes

The EA force of the EAS actuator can be tuned by adjusting the excitation voltage. When the bending moment caused by EA force is sufficiently high, the actuator maintains a fixed bending angle regardless of air pressure changes (locking mode). Conversely, under lower EA force, the bending angle is primarily determined by air pressure (sensing mode).

To evaluate the discharge response time of the EAS actuators, an experiment was conducted with the actuator integrated into the pneumatic actuator's skeleton. One electrode film was fixed to the skeleton, while the other was free and connected to a 200 g weight. The top of the skeleton was suspended from a force sensor (Futek, 1092619-2 lb). When a 1500 V, 50 Hz, 100% duty cycle voltage was applied, the electrodes adhered, suspending the weight. Upon voltage removal, the EA force vanished, causing the free electrode and weight to fall. The response time was measured based on the change in force sensor output.

Experiments showed that the EAS actuator with Type A structure exhibited high EA force density but a long discharge response time of 292 ms (Fig. 9). After applying high-voltage, high-duty-cycle excitation, significant electrostatic residuals remained, causing the actuator layers to stay adhered even after voltage removal. In contrast, the Type B actuator, using only

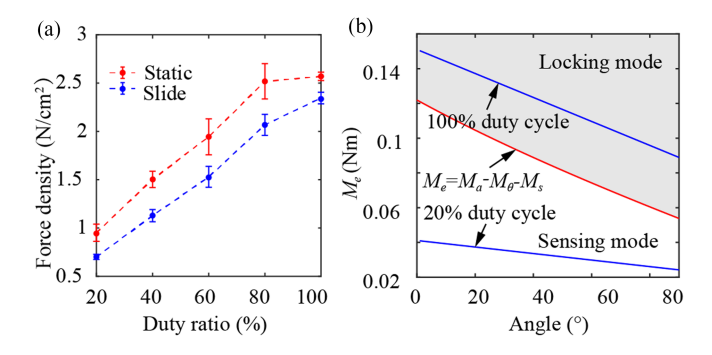


Fig. 10. The force analysis during the stiffness change. (a) The maximum tangential EA force density of the EAS actuator with Type B structure under different duty cycle of the excitation voltage (1500 V, 50 Hz). (b) The bending moment M_e required by the pneumatic actuator under different bending angle.

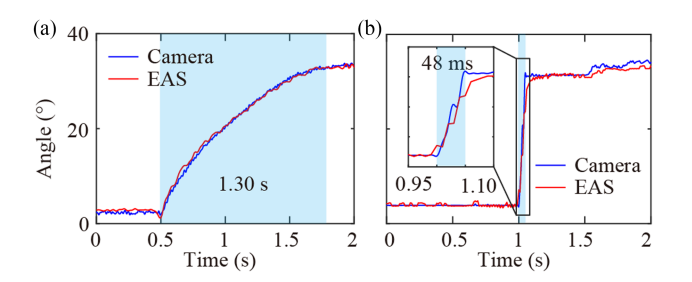


Fig. 11. The response time of the EAS pneumatic actuator with two actuation strategies: (a) Pneumatic only and (b) EA and pneumatic hybrid actuation.

PI as the dielectric, showed a much faster response. Its layers separated quickly after voltage cutoff, with a discharge time of 136 ms, only 46.6% that of the Type A actuator (Fig. 9).

To enable switching between locking and sensing modes, the excitation voltage and duty cycle must be carefully selected. As shown in Fig. 10(a), the maximum EA force densities of the Type B actuator (with PI dielectric) were measured under 1500 V, 50 Hz excitation at varying duty cycles. The resulting bending moment $M_e(\theta)$ derived from $F_t(\theta)$ using equation (14), determines whether the actuator locks or remains flexible; at 100% duty cycle, the EA force density reaches 2.57N/cm², and $M_e > M_a - M_\theta - M_s$, ensuring actuator locking. At 20% duty cycle, $M_e < M_a - M_\theta - M_s$, allowing free motion (Fig. 10(b)). Based on these results, the locking mode is defined as 1500 V, 50 Hz, 100% duty cycle, and the sensing mode as 1500 V, 50 Hz, 20% duty cycle.

D. Fast Response Actuator Test

A rapid-response pneumatic actuator was realized using the Type B EAS actuator. First, the response time of a pneumatic actuator controlled solely by air pressure was tested. The actuator was connected to a solenoid valve (Dehnker, 24 V DC, 1.8 W) via a silicone tube (inner diameter 2 mm, outer diameter 4 mm), with the valve linked to a proportional valve (SMC, IT1030-312 L) for pressure regulation. The EAS actuator operated at 1500 V, 50 Hz, with a 20% duty cycle, and bending was controlled by switching the solenoid valve. Upon valve opening, air from the 60 kPa source flowed into the actuator, which reached a 35° bend in 1.3 s due to system constraints such as tubing diameter (Fig. 11(a)).

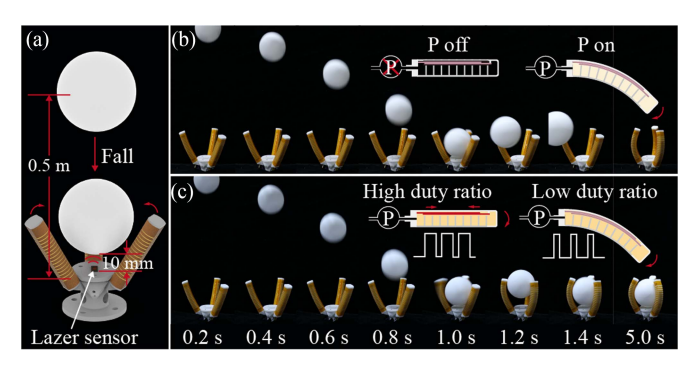


Fig. 12. The screenshots of the three-fingered gripper catch a falling ball. (a) Schematic diagram of the experiment. (b) Pressure control only. (c) Pressure and EAS actuator hybrid control.

In contrast, with the EAS actuator actively regulating stiffness, the response time improved significantly. Before actuation, a 100% duty cycle excitation ($1500\,\mathrm{V}, 50\,\mathrm{Hz}$) was applied to lock the actuator under $60\,\mathrm{kPa}$ pressure. Upon switching to 20% duty cycle, the actuator rapidly bent to 35° within $48\,\mathrm{ms}$ (Fig. 11(b)), demonstrating a substantial enhancement in response speed.

E. Three Fingers Gripper Test

A three-fingered gripper was developed based on the fastresponse pneumatic actuator. As shown in Fig. 12(a), when the ball approaches within 10 mm of the gripper base, the laser sensor located at the bottom responds and triggers the pneumatic gripper to grasp the object. In the first scenario (Fig. 12(b), Video S1), the actuator was connected to a 60 kPa air source via a solenoid valve. Upon detecting the falling ball (PLA, 80 mm diameter, dropped from 0.5 m), the valve opened; however, due to airflow delay, the actuator took about 4 s to close, and the ball bounced away before grasping. In the second scenario (Fig. 12(c), Video S1), the actuator was pre-pressurized (60 kPa) and held at its initial position by applying a 100% duty cycle voltage (1500 V, 50 Hz). Upon detection, the duty cycle was reduced to 20%, lowering the EA force and switching to the sensing mode. This enabled rapid bending within 40 ms, allowing successful ball capture.

After the rapid grasping response, the actuator's stiffness can be continuously adjusted via the duty cycle (e.g., higher stiffness for stable holding, lower stiffness for release; see Video S2). In the demonstration, the gripper first quickly grasps the ball. The duty cycle is then increased to 80% to reinforce stiffness, ensuring a firm grip. To release the object, the duty cycle is reduced to 20%, lowering the stiffness. As a result, the gripper can no longer resist the internal air pressure and the ball is released.

F. 2-DOFs Actuator Test

By adjusting the EA force, the stiffness of pneumatic actuators can be actively modulated. Using the switching between locking and sensing modes, multiple actuators can be serially controlled using a single air source, significantly reducing pneumatic components and enabling lightweight system design. In the experiment (Fig. 13, Video S3), two pneumatic actuators

Actuator	Sensor material	Sensing method	Accuracy	Stiffness varia- tion method	Stiffness varia- tion Ratio	Variation speed
B. Fang et al. [25]				LJ	6×	<2 s
S. Jadhav et al. [26]				FJ	8×	<1 s
A. Pagoli et al. [27]	No sensing functionality			MF	4×	<1 ms
W. Wang et al. [28]				SMA	55×	240 s
T. Wen et al. [29]				LMPA	6×	30 s
Y. Hao et al. [30]	EGaIn	Resistance	Nonlinear	LMPA	36×	12 s
H. Liu et al. [31]	Melt LMPA	Resistance	Nonlinear	LMPA	158×	3 s
A. Firouzeh et al. [32]	Constantan Serpantine	Resistance	$\pm 2.4^{\circ}$	SMP	40×	\sim
Z. Xu et al. [33]	CNTs	Resistance	\sim	SMP	600×	200 s
T. Hainsworth et al. [34]	Carbon Black PLA	Resistance	10% error			
Y. Cao et al. [35]	Microfilament	Resistance	10% linearity	No stiffness modulation functionality		
S. Kim et al. [36]	AgNWs	Capacitance	$R^2 = 0.9957$			
R. Nur et al. [37]	Gold Films	Capacitance	$R^2 = 0.98$			
Y. Ai et al. [38]	Helical Coils	Inductance	$R^2 = 0.99$			
This Work	Parallel Electrodes	Capacitance	4.92% linearity	EA	4.66×	20 ms

TABLE I
COMPARISON OF ACTUATORS WITH SENSING AND STIFFNESS MODULATION CHARACTERISTICS

LJ: Layer Jamming, FJ: Fiber Jamming, MF: Magnetorheological Fluids, SMA: Shape memory alloy, LMPA: Low melting point alloy, SMP: Shape memory polymer.

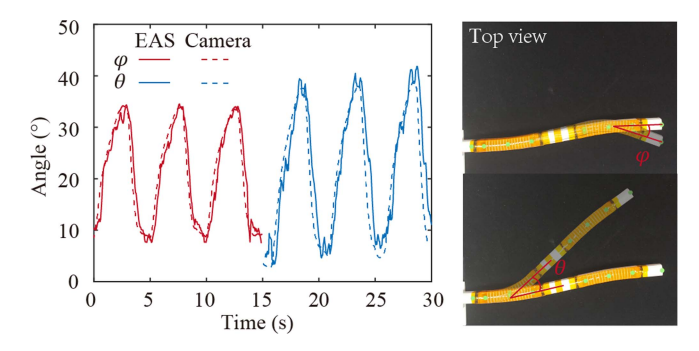


Fig. 13. The 2-DOFs arm test.The comparison between the bending angle from the EAS actuator and the visual algorithm.

were connected in series and placed horizontally. One actuator operated in locking mode (1500 V, 50 Hz, 100% duty cycle), while the other was in sensing mode (1500 V, 50 Hz, 20% duty cycle). By regulating air pressure via a proportional valve, only the sensing-mode actuator bent, while the locking-mode actuator remained stationary. Throughout the process, the EAS actuator provided real-time angle sensing, while a vision system was used to independently verify the accuracy of the sensing results.

V. DISCUSSION

We compared flexible actuators with various stiffness modulation methods and self-sensing strategies (Table 1). While many actuators excel in either stiffness modulation or self-sensing, achieving both fast stiffness tuning and accurate sensing in a single system remains challenging due to inherent trade-offs (e.g., between response speed and sensing linearity). In contrast, the EA-based approach in this study offers a well-balanced solution, combining rapid stiffness modulation with high sensing linearity.

Traditional EA brakes typically perform specific functions merely by controlling the EA force. In contrast, this study combines EA force control with position measurement, based on the principle that the capacitance of a parallel-plate capacitor

varies with changes in the overlapping area. Regarding EA force control, instead of the conventional approach of regulating the excitation voltage amplitude, this work controls the EA force by adjusting the duty cycle of the square wave excitation voltage. This method facilitates rapid response and miniaturization. Moreover, the linear relationship between the duty cycle and the EA force simplifies the control process. By integrating the EAS actuator with a pneumatic actuator, stiffness control and fast response of the pneumatic actuator are realized. To verify the fast-grasping capability of the actuator, a three-fingered gripper was fabricated, which successfully caught the falling ball in 40 ms. Additionally, a 2-DOFs pneumatic arm was constructed by connecting two pneumatic actuators in series to a single air source. Decoupling control of the 2-DOFs pneumatic arm was achieved by alternately modulating the stiffness of the actuators. This provides a novel approach for developing lightweight multi-DOFs pneumatic robots. Despite these achievements, the current actuator has limitations. The displacement accuracy of the sensor (4.92% linearity) and the sampling frequency (50 Hz) can be improved.

VI. CONCLUSION AND FUTURE WORK

This letter presents an EAS actuator capable of measuring displacement while achieving force regulation without adding additional sensor components. Moreover, when integrated with a pneumatic system, it enables the development of a self-sensing pneumatic actuator that can regulate stiffness and respond rapidly. By using the switching between the locking and sensing modes, the control of a multi-DOFs pneumatic robot using a single air source is realized. This research provides a novel concept for the miniaturization and lightweight design of pneumatic robots, opening up new possibilities in the field of soft robotics.

In the future, the research may focus on achieving untethered actuation of the actuator through circuit lightweight design. This could enable applications in weight-sensitive scenarios, such as aerial vehicles. Furthermore, sensing accuracy and frequency can be improved by optimizing the circuit design, implementing

electromagnetic shielding, and selecting high-frequency semiconductor devices. Moreover, a laminated design can be adopted to expand the stiffness variation ratio, enabling the actuator to be applied in a wider range of application scenarios such as flexible wearable exoskeletons, agricultural picking robots, and surgical robots.

REFERENCES

- [1] D. Wei et al., "Electrostatic adhesion clutch with superhigh force density achieved by MXene-poly(vinylidene fluoride-trifluoroethylene-chlorotrifluoroethylene) composites," *Soft Robot.*, vol. 10, no. 3, pp. 482–492, Jun. 2023.
- [2] E. W. Schaler, D. Ruffatto, P. Glick, V. White, and A. Parness, "An electrostatic gripper for flexible objects," in *Proc. IEEE/RSJ Int. Conf. Intell. Robots Syst.*, Vancouver, BC, Canada, Sep. 2017, pp. 1172–1179.
- [3] J. Guo, J. Leng, and J. Rossiter, "Electroadhesion technologies for robotics: A comprehensive review," *IEEE Trans. Robot.*, vol. 36, no. 2, pp. 313–327, Apr. 2020.
- [4] G. Hwang, J. Park, D. S. D. Cortes, K. Hyeon, and K.-U. Kyung, "Electroadhesion-based high-payload soft gripper with mechanically strengthened structure," *IEEE Trans. Ind. Electron.*, vol. 69, no. 1, pp. 642–651, Jan. 2022.
- [5] S. Diller, C. Majidi, and S. H. Collins, "A lightweight, low-power electroadhesive clutch and spring for exoskeleton actuation," in *Proc. IEEE . Int. Conf. . Robot. . Automat.*, Stockholm, Sweden, May 2016, pp. 682–689.
- [6] C. Chen, D. Fan, H. Ren, and H. Wang, "Comprehensive model of laminar jamming variable stiffness driven by electrostatic adhesion," *IEEE/ASME Trans. Mechatron.*, vol. 29, no. 3, pp. 1670–1679, Jun. 2024.
- Trans. Mechatron., vol. 29, no. 3, pp. 1670–1679, Jun. 2024.
 [7] F. Caro and M. G. Carmichael, "A review of mechanisms to vary the stiffness of laminar jamming structures and their applications in robotics," Actuators, vol. 13, no. 2, Feb. 2024, Art. no. 64.
- [8] T. Wang, J. Zhang, Y. Li, J. Hong, and M. Y. Wang, "Electrostatic layer jamming variable stiffness for soft robotics," *IEEE/ASME Trans. Mechatron.*, vol. 24, no. 2, pp. 424–433, Apr. 2019.
- [9] C. Chen, H. Ren, and H. Wang, "Augment laminar jamming variable stiffness through electroadhesion and vacuum actuation," *IEEE Trans. Robot.*, vol. 41, pp. 819–836, 2025.
- [10] D. J. Levine, G. M. Iyer, R. Daelan Roosa, K. T. Turner, and J. H. Pikul, "A mechanics-based approach to realize high–force capacity electroadhesives for robots," *Sci. Robot.*, vol. 7, no. 72, Nov. 2022, Art. no. eabo2179.
- [11] H. Imamura, K. Kadooka, and M. Taya, "A variable stiffness dielectric elastomer actuator based on electrostatic chucking," *Soft Matter*, vol. 13, no. 18, pp. 3440–3448, 2017.
- [12] R. J. Hinchet and H. Shea, "Glove- and sleeve-format variable-friction electrostatic clutches for kinesthetic haptics," Adv. Intell. Syst., vol. 4, no. 12, 2022, Art. no. 2200174.
- [13] A. Hajj-Ahmad, A. K. Han, M. A. Lin, G. H. Glover, and M. R. Cutkosky, "An electrostatically actuated gecko adhesive clutch," *Adv. Mater. Technol.*, vol. 8, no. 12, 2023, Art. no. 2202025.
- [14] D. Lee, H. Yu, and J. Bae, "Development of a soft semi-active suit using electro-static clutches for assisting static holding tasks," *IEEE Robot. Autom. Lett.*, vol. 9, no. 3, pp. 2814–2821, Mar. 2024.
- [15] C. Hegde, J. Su, J. M. R. Tan, K. He, X. Chen, and S. Magdassi, "Sensing in soft robotics," ACS Nano, vol. 17, no. 16, pp. 15277–15307, Aug. 2023.
- [16] G. Rizzello, P. Serafino, D. Naso, and S. Seelecke, "Towards sensorless soft robotics: Self-sensing stiffness control of dielectric elastomer actuators," *IEEE Trans. Robot.*, vol. 36, no. 1, pp. 174–188, Feb. 2020.
- [17] H. Wang, M. Totaro, and L. Beccai, "Toward perceptive soft robots: Progress and challenges," Adv. Sci., vol. 5, no. 9, 2018, Art. no. 1800541.

- [18] Q. Xiong et al., "So-eaglove: Vr haptic glove rendering softness sensation with force-tunable electrostatic adhesive brakes," *IEEE Trans. Robot.*, vol. 38, no. 6, pp. 3450–3462, Dec. 2022.
- [19] C. Liu, J. J. C. Busfield, and K. Zhang, "An electric self-sensing and variable-stiffness artificial muscle," *Adv. Intell. Syst.*, vol. 5, no. 9, 2023, Art. no. 2300131.
- [20] I. Choi, S. J. Yoon, and Y.-L. Park, "Linear electrostatic actuators with moiré-effect optical proprioceptive sensing and electroadhesive braking," *Int. J. Robot. Res.*, vol. 43, no. 5, pp. 646–664, Apr. 2024.
- [21] J. Santoso, E. H. Skorina, M. Salerno, S. De Rivaz, J. Paik, and C. D. Onal, "Single chamber multiple degree-of-freedom soft pneumatic actuator enabled by adjustable stiffness layers," *Smart Mater. Struct.*, vol. 28, no. 3, Mar. 2019, Art. no. 35012.
- [22] R. Hinchet and H. Shea, "High force density textile electrostatic clutch," Adv. Mater. Technol., vol. 5, no. 4, Apr. 2020, Art. no. 1900895.
- [23] T. Nakamura and A. Yamamoto, "Modeling and control of electroadhesion force in dc voltage," ROBOMECH J., vol. 4, no. 1, Dec. 2017, Art. no. 18.
- [24] P. Polygerinos et al., "Modeling of soft fiber-reinforced bending actuators," IEEE Trans. Robot., vol. 31, no. 3, pp. 778–789, Jun. 2015.
- [25] B. Fang et al., "Multimode grasping soft gripper achieved by layer jamming structure and tendon-driven mechanism," *Soft Robot.*, vol. 9, no. 2, pp. 233–249, 2022.
- [26] S. Jadhav, M. R. A. Majit, B. Shih, J. P. Schulze, and M. T. Tolley, "Variable stiffness devices using fiber jamming for application in soft robotics and wearable haptics," *Soft Robot.*, vol. 9, no. 1, pp. 173–186, 2022.
- [27] A. Pagoli, M. Alkhatib, and Y. Mezouar, "A soft variable stiffness gripper with magnetorheological fluids for robust and reliable grasping," *IEEE Robot. Autom. Lett.*, vol. 9, no. 5, pp. 4519–4526, May 2024.
- [28] W. Wang and S.-H. Ahn, "Shape memory alloy-based soft gripper with variable stiffness for compliant and effective grasping," Soft Robot., vol. 4, no. 4, pp. 379–389, 2017.
- [29] T. Wen, J. Hu, X. Li, and S. Kang, "A wide range of multi-stage stiffness regulation via harnessing phase variability of low-meltingpoint alloy," *IEEE Robot. Autom. Lett.*, vol. 9, no. 7, pp. 6664–6671, Jul. 2024.
- [30] Y. Hao et al., "A eutectic-alloy-infused soft actuator with sensing, tunable degrees of freedom, and stiffness properties," *J. Micromech. Microeng.*, vol. 28, no. 2, 2018, Art. no. 24004.
- [31] H. Liu et al., "Shape-programmable, deformation-locking, and self-sensing artificial muscle based on liquid crystal elastomer and low-melting point alloy," Sci. Adv., vol. 8, no. 20, 2022, Art. no. 5722.
- [32] A. Firouzeh, M. Salerno, and J. K. Paik, "Stiffness control in under-actuated robotic origamis with shape memory polymer," *Trans. Robot.*, vol. 33, no. 4, pp. 765–777, Aug. 2017, [Online]. Available: https://api.semanticscholar.org/CorpusID
- [33] Z. Xu et al., "Self-sensing actuators based on a stiffness variable reversible shape memory polymer enabled by a phase change material," ACS Appl. Mater. Interfaces, vol. 14, no. 19, pp. 22521–22530, 2022.
- [34] T. Hainsworth, L. Smith, S. Alexander, and R. MacCurdy, "A fabrication free, 3 d printed, multi-material, self-sensing soft actuator," *IEEE Robot. Autom. Lett.*, vol. 5, no. 3, pp. 4118–4125, 2020.
- [35] Y. Cao and J. Dong, "Self-sensing and control of soft electrothermal actuator," *IEEE/ASME Trans. Mechatron.*, vol. 26, no. 2, pp. 854–863, 2020.
- [36] S.-R. Kim, J.-H. Kim, and J.-W. Park, "Wearable and transparent capacitive strain sensor with high sensitivity based on patterned ag nanowire networks," ACS Appl. Mater. Interfaces, vol. 9, no. 31, pp. 26407–26416, 2017.
- [37] R. Nur, N. Matsuhisa, Z. Jiang, M. O. G. Nayeem, T. Yokota, and T. Someya, "A highly sensitive capacitive-type strain sensor using wrinkled ultrathin gold films," *Nano Lett.*, vol. 18, no. 9, pp. 5610–5617, 2018.
- [38] Y. Ai et al., "Robust fiber strain sensor by designing coaxial coiling structure with mutual inductance effect," *Adv. Fiber Mater.*, vol. 6, no. 5, pp. 1629–1639, 2024.